Differentiation of Vascular Characteristics Using Contrast-Enhanced Ultrasound Imaging

Ultrasound in Med. & Biol., Vol. 45, No. 9, pp. 2444–2455, 2019

0301-5629/$ - see front matter

https://doi.org/10.1016/j.ultrasmedbio.2019.05.015

● *Original Contribution*

DIFFERENTIATION OF VASCULAR CHARACTERISTICS USING CONTRAST-ENHANCED ULTRASOUND IMAGING

Mairead Butler,* Antonios Perperidis,† Jean-Luc Matteo Zahra,‡ Nadia Silva,§ Michalakis Averkiou,¶ W. Colin Duncan,‖ Alan McNeilly,‖ and Vassilis Sboros*

* Heriot-Watt University, Institute of Biochemistry, Biological Physics and Bio Engineering, Riccarton, Edinburgh, UK; † Heriot-Watt University, Institute of Signals, Sensors and Systems, Riccarton, Edinburgh, UK; ‡ Heriot-Watt University, Department of Physics, Riccarton, Edinburgh, EH14 4 AS, UK; § Centre for Marine Sciences, University of Algarve Faro, Portugal; ¶ Department of Bioengineering, University of Washington, Seattle, WA 98195, USA; and ‖ Centre for Reproductive Health, University of Edinburgh, Edinburgh, UK

(*Received* 21 *August* 2018; *revised* 2 *May* 2019; *in final from* 10 *May* 2019)

Abstract—Ultrasound contrast imaging has been used to assess tumour growth and regression by assessing the flow through the macro- and micro-vasculature. Our aim was to differentiate the blood kinetics of vessels such as veins, arteries and microvasculature within the limits of the spatial resolution of contrast-enhanced ultrasound imaging. The highly vascularised ovine ovary was used as a biological model. Perfusion of the ovary with SonoVue was recorded with a Philips iU22 scanner in contrast imaging mode. One ewe was treated with prostaglandin to induce vascular regression. Time-intensity curves (TIC) for different regions of interest were obtained, a log-normal model was fitted and flow parameters calculated. Parametric maps of the whole imaging plane were generated for 2 × 2 pixel regions of interest. Further analysis of TICs from selected locations helped specify parameters associated with differentiation into four categories of vessels (arteries, veins, medium-sized vessels and micro-vessels). Time-dependent parameters were associated with large veins, whereas intensity-dependent parameters were associated with large arteries. Further development may enable automation of the technique as an efficient way of monitoring vessel distributions in a clinical setting using currently available scanners. (E-mail: m.butler@hw.ac.uk)

Key Words: **Ultrasound, Contrast agent, Microbubble, Capillary, Vessel imaging.**

INTRODUCTION

Contrast-enhanced ultrasound (CEUS) imaging is an expanding field with a wide range of current and potential applications. One area yet to fully benefit from the potential of ultrasound contrast agents is the imaging of the microcirculation. Very narrow and evolving blood vessels are found in tumour vasculature (Folkman 2003) and angiogenesis within atherosclerosis (Moreno et al. 2006), with their structure, development and appearance being useful diagnostic markers. Positron emission tomography scanning currently can distinguish between the malignant and non-malignant tissue by enabling quantification of macroscopic flow (Dijkmans et al. 2006; El-Galaly et al. 2018). However, the high cost and associated radiation hazard render it largely impractical for significant clinical use, particularly for repetitive monitoring of treatment. Contrast-enhanced magnetic resonance imaging (MRI) also has the capability of providing flow information on micro-vessels within tumours (Lagaru and Gambhir 2013; Simoncic et al. 2017). However, MRI contrast agents do not just remain within the vasculature; a proportion of the agent distributes to the extracellular spaces, thus enabling the evaluation of vascular permeability instead of providing vascular flow assessment (Mori et al. 2017).

Ultrasound contrast agents are blood pool agents and unable to pass into the extracellular spaces making them ideal markers for assessing blood flow through micro-vessels (Mori et al. 2017). In general, a very large number of diseases have altered blood flow, which directly links to the pathophysiology and the progression

Address correspondence to: Mairead Butler, Heriot-Watt University, Institute of Biochemistry, Biological Physics and Bio Engineering, Nasmyth Building, Riccarton, Edinburgh, EH14 4 AS, UK. E-mail: m.butler@hw.ac.uk

of the disease. Dynamic CEUS has been shown to have potential in the assessment of perfusion of microvascular structures such as tumours. Time-intensity curve (TIC) analysis appears promising in assessing tumour therapy using anti-angiogenic agents (Lassau et al. 2014; Lassau et al. 2012) where the area under the curve (AUC) was shown to be the most significant indicator of tumour stability when the whole tumour was selected as the region of interest (ROI) (Lassau et al. 2014). However, to date the research in conventional CEUS approaches has not produced quantitative vascular indices that are clinically robust. The recent advances in super-resolution imaging (SRI) provide maps of the structure and dynamics of the vascular bed with resolution that potentially can exceed 10-fold that of CEUS. Initial work on *in vivo* animal models (Christensen-Jeffries et al. 2015; Errico et al. 2015) has been followed by the potential identification of tumour characteristics (Opacic et al. 2018). The method deploys microbubble (MB) localization similar to that utilised in region localisation in fluorescent optical microscopy or astronomy. Given that this method works through single microbubble localisation, and there are large numbers of vessels in view (*e.g.,* in a 2-D CEUS image plane), all vessels need to be crossed several times by single microbubbles. This is challenging because only a few isolated microbubbles can fit in an image. The vascular network imposes another restriction. Vessels of different diameters, from micrometers to centimeters, provide a large variation in vascular volume and consequently orders of magnitude variations in microbubble density. In practice, achieving a few single microbubbles in the microvasculature may require a high-density microbubble population from the millimetre-sized vessels that supply these. This means that millimetre-sized vessels would not have distinguishable single microbubbles for super-resolution processing. On the other hand, the reduction of microbubble concentration results in a significant increase in the required image data required for recovering the vascular structure in view, which translates into clinically impractically long examination times. Further, because larger vessels contain larger MB concentrations, the likelihood of multiple or overlapping MB echoes increases and the MB localisation and tracking may be compromised. In addition, it is difficult at this stage to envisage single emission (Errico et al. 2015) protocols useful for imaging entire organs. This is because the acoustic pressure varies significantly across the image and this introduces a variable MB density (Sboros et al. 2003). As a consequence, the link between MB count and vascular volume is variable. Focused transmission may ensure a less variable acoustic pressure field across an image, higher depth penetration and thus the potential, through SRI, to provide good representation of the vasculature of entire organs. The microbubble transit time physically imposes the minimum duration for the vascular bed to be mapped. Bolus injections of microbubbles take a few minutes to partially washout; therefore, to maintain an examination time of a few minutes, it is likely that a larger concentration is needed at least for the larger vessels in view.

The tracking of microbubbles may not be the only method that provides improved resolution. Recently methods deploying pixel dynamics have shown significant promise in capturing vascular structure in high resolution (van Sloun et al. 2018; van Sloun et al. 2019), although not as much as SRI. Vessels that are usually above the resolution limit may significantly benefit from such methods. The conventional method of investigating these is through parametric mapping.

The first parametric maps were provided by the visualisation of vascular structure using maximum intensity projection. The maximum intensity of each pixel over a number of consecutive frames is displayed in a meta-image, enabling the highlighting of the contrast agent path and thus the structure of the vessels (Forsberg et al. 2011). Generally, in CEUS, parametric mapping refers to images where each pixel provides the value of a parameter as fitted to the TIC of the particular pixel (Greis 2011). The method appears to provide more quantitative results on tissue disease state (Dizeux et al. 2017). This approach has evolved to mapping parameters not directly derived from the TIC, but the result of a more complex calculation of a physical parameter, a candidate biomarker, associated with the vascular expression of pathology. Such are the diffusion and dispersion parameters that provide biomarkers for tumours and have shown to be superior to TIC-derived parameters (Kuenen et al. 2011; Kuenen et al. 2013). A significant advance, similar to the concept of microbubble tracking is a direct translation of diffusion tensor tractography in MRI into 3-D vascular imaging by ultrasound tractography (van Sloun et al. 2018). The fractal dimension representing wash in rate and peak intensity (Ip) determined from dynamic CEUS was used to differentiate between two prostate cancer models comprising different microvascular structures (Saidov et al. 2016). All these studies demonstrate significant potential in revealing abnormal vascular dynamics using CEUS. Importantly, they demonstrate that the pixel statistics may be important to improving resolution and image sensitivity. The underlying reasons for making some of these methods work better than others are not fully clarified, partly because it is difficult to have good quality ground truth in *in vivo* investigations. Most of ground truth currently relies in histologic or other non-live evaluation.

Although all these methods enable the visualisation of vascular-related parameters, there is still little

knowledge available on the type or approximate size of the vessels that this information originates from. To date there is no study that investigates the ability of conventional CEUS to detect different sizes of vessels. This is the subject of the investigation in this article.

The distinction between large vessels and the rest of the vasculature using frame sequences from ultrasound contrast imaging of the ovine corpus luteum (CL) (Perperidis et al. 2014) demonstrated the ability to differentiate between large vessels and the rest of the vasculature using frame sequences from ultrasound contrast imaging of the ovine CL. This article further investigates the differentiation of different sized vessels. The ovine CL provides a suitable *in vivo* model as different vessel sizes can be found at different locations in the image plane. The CL is a transient vascular structure on the ovary with a complex microvascular bed responsible for progesterone secretion. In maturity, it is an approximately spherical structure of 0.5−2 cm in diameter, comparable in size to a small tumour, and is suitable for developing CEUS methodology (Sboros et al. 2011; Strouthos et al. 2010). It is also a model to study vascularisation because its generation and regression are predictable and can be synchronised (Fraser and Duncan 2009). The ovary contains a network of larger vessels that branch out of the ovarian artery and cover the periphery of the CL. Within the CL itself, there is a high-density microvascular network such that each luteal cell is in direct contact with an endothelial cell (Fraser and Duncan 2009). Thus, the centre of the CL is nearly entirely composed of capillaries and venules, providing a large ROI in the ultrasound imaging plane that is dominated by the microvascular bed, representing a hi-fidelity *in vivo* biological model of microvascular flow. The CL microvasculature then feeds into the venous system which is spatially located alongside the arterial feeds. This means that the CL containing ovary is particularly suitable for imaging ROIs containing different sized vessels and for the implementation of parametric mapping methodology to enable vessel differentiation. Our aim here was to investigate this distinction to allow more specific identification of veins, small and large arteries and capillaries, using the CL within the ovary as an *in vivo* biological model of vascular flow. In a comprehensive study of all TIC parameters, new criteria for differentiating vessel types within the resolution of CEUS were developed. Finally, vascular regression within the CL was imaged, in a proof-of-principle attempt to demonstrate the ability to map changes in microvasculature. The results have implications in understanding the uncertainties associated with CEUS analysis and may work synergistically to recent SRI methodologies to boost CEUS resolution.

METHODS

Contrast ultrasound imaging

As mentioned above, the CL-containing ovine ovary was used as a model for a highly vascularised system, where large and small blood vessels could be imaged together in one imaging plane. The methods have been previously described (Sboros et al. 2011). In short, ewes (n = 11) were synchronised to the mid luteal phase using standard animal husbandry methods using progesterone sponge administration and prostaglandin, prostaglandin F2 alpha (PGF2α) administration. About 10 d after sponge withdrawal ewes were anaesthetised and their ovaries exposed, with a fully maintained blood supply, by laparotomy and covered in scanning gel to allow fixed plane scanning. This method provided a vascular source where optimal data from the contrast agent could be recorded without loss of information due to sheep anatomy or inability to achieve a good image plane. To assess proof of concept one ewe had an injection of PGF2α (0.5 mL prostaglandin estrumate; Schering Plough Animal Health, Welwyn Garden City, UK) 24 h before scanning. This causes a predictable and marked reduction in microvascular density (Baird and McNeilly 1981; Sboros 2014; Vonnahme et al. 2006). For the study presented here it provided a data set with a regressed vasculature to show how differences and changes in vasculature may potentially be assessed.

Using 2.4 mL bolus injections of Sonovue (Bracco, Geneva, Switzerland) followed by 5-mL saline, videos were acquired of the contrast agent through wash-in, Ip and wash out phases. Each bolus injection contained between 2.4 and 12 $\times$ 10^8 microbubbles. A Philips iU22 ultrasound scanner (Philips Medical Systems, Bothell, WA, USA) with a L9-3 linear array probe was used for all imaging with mechanical index 0.05. Recording commenced at the same time the saline flush was administered. Dual image b-mode and contrast mode videos were acquired. Multiple videos for each ovary were recorded, and Doppler scans provided additional information on the larger blood vessels. In total, 23 contrast videos of individual bolus injections, from 11 different ovaries were available for the study presented here. The videos were saved and exported from the scanner in DICOM format. After scanning, each sheep was euthanised and the ovaries removed and fixed for histologic analysis. All surgical work was conducted under UK Home Office approval (Project Licence McNeilly PPL 60/3906).

Histology

Ovaries were fixed in Bouin's solution for 8 h and embedded in paraffin wax. Sections (5 μm thick) were cut, de-waxed, rehydrated and antigen retrieval was

achieved for 20 min in a pressure cooker using citrate buffer 0.01 M. Endogenous peroxidase was inactivated by immersion in a solution of 3% H_2 O_2 in methanol for 20 min followed by avidin and biotin blocking (Vector Labs, UK). Biotinylated Lectin BS-1 (Sigma, UK), used to specifically bind to endothelial cells, was diluted 1/80 in normal goat serum (NGS)/Tris-buffered saline (TBS)/ 5% bovine serum albumin (BSA) and applied overnight to tissue sections at 4˚C in a humidified chamber. Detection was performed for 30 min at room temperature using streptavidin-HRP (Vector Labs) diluted 1/1000 in NGS/TBS/5% BSA. Development of signal was made using Impact diaminobenzidine (Vector Labs) to stain the endothelial cells brown and identify vessels. Sections were washed, dehydrated and mounted using Pertex. The section that was a close to the ultrasound image plane as possible was chosen the represent the ROI and was analysed using a light microscope (Olympus BH2) coupled to a digital camera for image capture. Vessels across the whole plane were measured and counted in order to determine the average vessel content of the cross section. Vessels were grouped into those less than 30 μm diameter, those which were 30−200 μm diameter and those which were greater than 200 μm diameter.

Analysis of contrast video data

Initial processing of large ROIs was performed in QLab (Philips Medical Systems) with Matlab (Mathworks, Natick, MA, USA) being used for further automated pixel processing (each pixel measuring 140 × 140 μm). In general, the parametric maps derived were of lower resolution compared to the original data (Kuenen et al. 2013). We tested 1 × 1 to 4 × 4 pixel ROIs and concluded that a 2 × 2 pixel ROI being the best compromise between resolution and good signal-to-noise ratio in the TIC curves, which in turn resulted in reproducible parametric data. For the videos, rigid movements of the ovary due to respiration had to be removed. To correct this, each frame in the acquired video was aligned to a reference frame, chosen at the end of a respiration cycle. To achieve the alignment, a Nelder and Mead's Simplex optimisation method (Lewis 1995; Nelder and Mead 1965) was used for derivation of the rigid transformation which maximised the normalized cross-correlation between the registered images (current frame to reference frame).

Parametric maps

Time-intensity curves are commonly used for analysing the flow of contrast agent in CEUS imaging (Dietrich et al. 2012). For example, Figure 1a shows example TICs obtained for a small region of interest (ROI A) within the CL, which was dominated by micro-vessels (arterioles, capillaries and venules), as well as for a

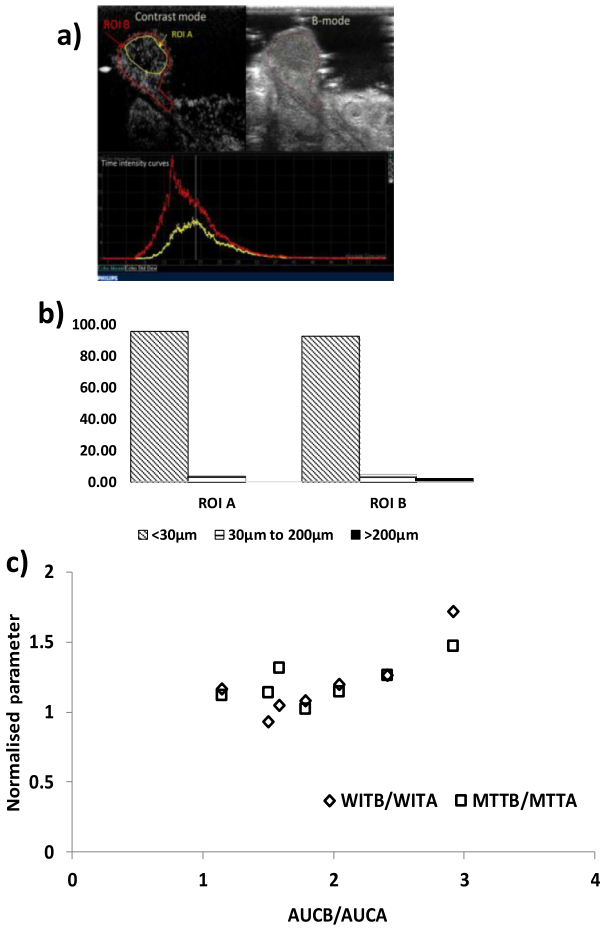

Fig. 1. (a) B-mode and contrast mode ultrasound images that show the location of) ROI A (yellow) and B (red) along with their corresponding time intensity curves. (b) % of vessels of different size ranges found in each region of interest. The histologic ROI B does not contain the larger vessels at the edge of the ROI because these are lost during tissue processing. (c) shows how the ratio of the MTT and wash in time (WIT) for ROIs A and B vary with AUC. ROI = region of interest (ROI); MTT = mean transit time; WIT = wash in time; AUC= area under the curve.

larger ROI B which covers the whole ovary and included the larger feeding vessels as well as the artery and vein that branch out into the respective ovarian vessels. For each TIC, a smoothing spline fit was used to remove high levels of noise. The resulting smoothed TIC was used to extract the flow- and volume-related parameters by fitting a Log-normal model. The following parameters were then calculated from the TICs: (i) Ip, (ii) time for the peak intensity (tp) to occur, (iii) mean transit time (MTT) of the contrast agent, (iv) wash in time (WIT) (time between 5% and 95% of Ip), (v) rate of increase during wash in (WIR) (5%−95% of Ip), (vi) wash out time (WOT) (time between 95% and 45% of Ip, a 50% drop), (vii) rate of decrease during wash out (WOR), (viii) area under the lognormal curve and (ix)

the regression coefficient of the data to the model (R^2) (Strouthos et al. 2010).

Following this, the TICs for 2 × 2 pixel ROIs over the entire scan plane were calculated. The TICs were then used to enable parametric mapping of the entire image plane. These maps provided localised information on individual curve parameters as generated by the lognormal model that was fitted to the local TIC. It was observed that regions of very-low-density contrast flow produced noisy data resulting in TICs from which some flow parameter values were overestimated due to the broad shape of the fitted TIC. This often created an erroneous outlying saturated parametric signal. To account for this, the parametric maps and TICs were inspected and ROIs with erroneous parameter estimation were assigned the lowest detectable intensity values for each parameter, respectively. These regions of very low flow were not used for the later location specific parametric analysis.

Reproducibility of TIC

For 11 different ROIs (four different ovaries), videos comprising two or three consecutive ultrasound contrast scans were selected. TICs for 2 × 2 pixel ROIs were chosen to be in regions of good contrast echo. The same ROI by pixel number was chosen in each set of consecutive videos. Parameters associated with the TIC were calculated for each curve. Mean, standard deviation and standard error were calculated for each group.

Comparison of vessel types

The parameter maps of the ovary indicated where the large veins and arteries and smaller vessel networks could be identified. Aided by the histologic analysis as well as prior knowledge of the vascular structure of the ovary and the parameter maps, TICs for 2 × 2 pixel ROIs from manually selected regions of specific vessel types were recalculated. These locations were chosen using (i) parametric maps of each ovary, (ii) histology, (iii) prior knowledge of the structure of the CL and ovary and (iv) user observations of the videos. The identifiable vessel types were arteries, veins, medium-sized vessels and micro-vessels. All the vessels greater than 200 μm in diameter were identified as "large," whereas micro-vessels were below 30 μm. All the vessels in between belonged to the "medium"-sized vessels grouping. These sizes were used in the histologic evaluation and do not directly refer to the interpretation of the ultrasound images. Given that the size of each pixel was 140 × 140 μm^2, the 2 × 2 pixel region was 280 × 280 μm^2. Thus, it was implied that the regions were dominated by the respective vessel type. For example, micro-vessel regions were those thought to be dominated by capillaries and may include larger vessels but was unlikely to include "large" vessels. Similarly, medium vessel regions were dominated by vessels between 30 and 200 μm, which may include capillaries, but did not include large vessels. In addition, arteries were identified as the regions to show the first inflow of contrast agent. Veins were similar in size and provided delayed contrast, which typically would appear at the same time or later compared to the inner microvascular CL and remained bright toward the end of the contrast perfusion. Medium-sized vessels were classified as filling and clearing in between the times of the large arteries and veins.

Time-intensity curves and all associated flow parameters were derived for the new 2 × 2 pixel ROIs. In total 54 ROIs associated with arteries, 35 ROIs associated with veins, 41 ROIs associated with medium-sized vessels and 67 ROIs associated with micro-vessels were selected. The same parameters were calculated and normalised to the intensity of the largest artery signal. From these, mean and standard deviation for each parameter associated with each vessel type were calculated because the distributions of these parameters were Gaussian. One-way analysis of variance (ANOVA) with a *post hoc* Tukey test (SPSS Statistics 25, IBM, Portsmouth, Hampshire, UK) were performed to determine if differentiation of the vessel types was achievable from flow characteristics of individual small ROIs.

RESULTS

Time intensity of the entire tissue

Figure 1a shows the TICs for the large overlapping ROIs. ROI A is within the CL and contains the smallest vessels in the ovary, whereas ROI B is the whole ovary which includes the entire CL structure with its vascular supply. ROI B (red) has the broadest TIC due to the largest veins and arteries that branch out from the ovarian artery and vein, and the main vessels which connect to the CL. In ROI A (yellow), the peak is lower than that of the ROI B because the region contains a higher proportion of smaller vessels and the bubble density is lower on average. Furthermore, ROI A has a narrower, later-to-peak curve as the smaller vessels fill after the feeding arteries and empty before the veins. On the other hand, ROI B produces a curve which is earlier to peak as the signal is dominated by the large arteries. These arteries have high concentrations of contrast and feed the vessels in the CL.

Histology

Figure 1b shows the relative proportions of vessels in different size ranges within two ROIs of the CL. The data presented are the mean of six ovaries from six different sheep. ROI A within the CL is primarily (95%) composed of vessels less than 30 μm diameter. For ROI B,

approximately 2% of the total vessel content are vessels which are larger than 200 μm diameter. These larger vessels are not located within ROI A, and the actual proportion of large vessels will be higher for ROI B when the larger vessels, removed during excising and processing, are included. Note, that although vessels larger than 200 μm are only 2% of the total vessel number, it is their volume that matters as the area they occupy in the ultrasound image and the blood volume within is largest, and thus, the contrast intensity is highest. This results in a much larger intensity for ROI B compared to ROI A in Figure 1a.

TIC parameters

Figure 1c shows the ratio of the MTT (ROI B)/MTT (ROI A) along with the same ratio for WIT and their correlation with the ratio for AUC (Averkiou et al. 2010). Both the MTT and WIT ratios have positive correlation coefficients with the AUC ratio (0.69 and 0.83, respectively). Based on this information it was concluded that the proportion of different vessels within a ROI impacts on the flow kinetic parameters derived from the fitted flow model. The larger ROI B provides larger intensity (AUC) and this appears to be associated with longer transit time (WIT and MTT). In general, transit time varies between different vessel sizes, as well as the starting time of the TIC of each vessel (*e.g.,* a vein TIC starts later than an artery TIC).

Because vessels of different type and size appear in the same image, it is expected that the TIC of any given ROI is a sum of the TICs of the different vessels that appear in the ROI. In the CL, ROI A is dominated by microvascular flow, whereas ROI B surrounding ROI A is dominated by medium to large vessel flow, thus providing a good initial knowledge on the locations of different vessel types. This leads to the hypothesis that conventional CEUS is able to provide information on flow behaviour of specific vessel types. This was further investigated using multiple, small regions of interest as follows.

Small TIC parametric analysis

TICs for small ROIs. Typical examples of TICs for 2 × 2 pixel ROIs are shown in (Fig. 2a–c). The best fit was seen in regions with the strongest signal (*i.e.,* the highest contrast concentration such as the supply arteries [Fig. 2a]); the artery ROI was chosen based on the first large vessel to fill in the ultrasound video. The worst log-normal fit was for micro-vessels less than 30 μm (Fig. 2c, 2d); the associated ROI was chosen from the highly microvascular central area of the CL. For low signal-to-noise TICs, as in Figure 2d, where parameters such as MTT are overestimated due to the broad, low shape of the fitted curve, the parametric images were adjusted accordingly. In particular, the region of overestimation was assumed to contain very small vessels where parameters were set to the minimum measurable value in the data set (*e.g.,* those which would be calculated from the curve type of Figure 2c).

The TICs for small ROIs within regions determined to be arteries and veins peak at different times as expected due to the flow dynamics through the ovary. The difference in mean MTT for 35 vein ROIs and 53 artery ROIs (from 13 different videos) was 3.1 ± 1.8 s. Similarly, for Tp, the difference between vein and artery ROIs was 3.7 ± 1.5 s.

There was good reproducibly between parameters calculated from TICs in consecutive videos of the same ovary. Table 1 shows the minimum and maximum mean values for each parameter, over all videos assessed, with the corresponding standard error.

Small TIC parametric mapping

Example parametric maps are displayed in Figure 3. The larger veins (blue arrow) and arteries (red arrow) are clearly seen toward the bottom of each image; the artery and vein were confirmed by surveying the video sequence. The area comprising smaller vessels is known to be the upper region and central region of the image plane. In Figure 3, the R^2 parameter map is consistently bright for the all vessel types apart from the smallest capillaries. It is also seen that the Ip, AUC, WIR and WOR values are higher in the large arteries (red arrow in Ip map), thus making the main arteries and other arterioles (yellow arrow) the dominant vessels in each respective map. On the other hand, for the MTT, WIT and WOT of the vein produce the dominant signal (blue arrow). Capillaries generally provide the lowest parameter values throughout apart from the MTT, where they fall within similar values to all other arteries.

Figure 4 illustrates the mean value for each parameter with error bar of one standard deviation across different vessel types. Significance for each parameter was determined by one-way ANOVA with a *post hoc* Tukey test used to identify the vessel groups between which there was significant difference. The vessel groups within each parameter which were significantly different ($p < 0.05$) are indicated. As with Figure 3 the bar chart highlights, with statistical significance, that the intensity-dependent parameters have artery dominant behaviour (Ip, AUC, WIR, WOR) and time-dependent parameters have vein dominant behaviour (MTT, WIT, WOT). The capillaries are also confirmed to have the lowest values in all parameters apart from the MTT. From the data it was determined that there are values and relative values of parameters which can be attributed to a specific vessel type.

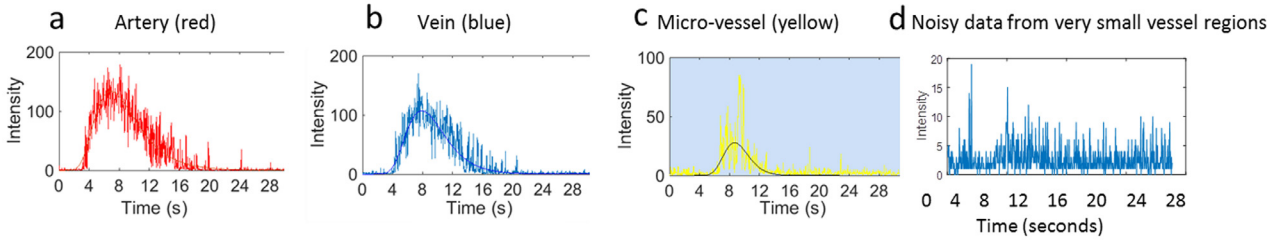

Fig. 2. Typical TIC for 2 × 2 pixel areas located in different vessel types, (a) artery (red TIC), (b) vein (blue TIC) and (c) small vessel (yellow TIC). It is seen that as the vessel decreases in size the TIC becomes less defined and more noisy. (d) is an example of a poorly defined TIC from a small vessel. For these due to the broad shape of the fitted curve flow, parameters were overestimated. As described, parameters associated with these TICs were corrected by being allocated the lowest measurable value for the specific parameter map. TIC = time-intensity curve.

Figure 5 shows the output from analysis for a further three different sheep ovaries including the one that has undergone vascular regression (CL4) including (a) the colour Doppler images, (b) the image from the peak contrast frame throughout the video, (c) the parameter map for Ip and (d) the tiled microscopy image (histologic evaluation) confirming the high vascular density within the region of the CL. The histology slices are in general agreement with the overall vascular structure shown in the ultrasound images. For each CL, the central area is densely populated with micro-vessels and larger vessels are found toward the outer region. Yet, it is well understood that a quantitative comparison between histologic slices and medical imaging data is not easy to achieve. However, there are several arrowed features (orange arrow) that confirm a strong similarity between the parametric maps and the histologic slices, mainly for the medium to large vessels. Although the resolution of the original CEUS is not fundamentally different from the parameter map, the latter provides some structure detail that is not distinguishable in the contrast video. On the other hand, visual inspection of the colour Doppler data, the current method for locating large blood vessels *in vivo,* provides cruder information on the location of the largest vessels, overestimating the actual size of the large vessels.

Figure 5 CL4 shows proof-of-principle data from an ovary which had been treated with prostaglandin to induce vascular regression of the CL. Of particular importance is the capillary dense area. In the normal CLs (Fig. 5 CL2 and CL3), vascular flow is depicted by the presence of a network of arteriolar flow (medium-sized vessels). From histology we know that only vessels less than 200 μm are located within the central region of the CL. The histology also shows that the vascular density is significantly decreased in the centre of the CL. Although small submillimetre cysts may appear in normal mature CLs, the size of the vacant space exceeds 3 mm. In the regressed CL this network is absent, thus making the inner CL area appear dark in the parameter map, indicating the absence of vessels in that region.

DISCUSSION

This study of time-intensity kinetics of ultrasound contrast demonstrates that vessel differentiation is possible within the standard resolution of CEUS. Our study confirms the work of others that makes use of TICs from single pixels to extract parameters which can be used to identify the nature of vascular structure (Kuenen et al. 2011; Kuenen et al. 2013; Pitre-Champagnat et al. 2015).

Table 1. Minimum and maximum mean values for each parameter calculated from repeat contrast ultrasound scans with the corresponding standard error

Parameters	Minimum mean	Standard error	Maximum mean	Standard error
AUC	11,590	2502	45,197	8266
FWHM	10.79	0.04	34.33	2.47
Ips	47.44	4.91	118.64	8.49
MTTs	17.57	1.30	43.41	1.88
R^2	0.78	0.11	1.00	0.00
Tps	13.63	2.79	35.22	0.74
WIRs	0.21	0.02	1.20	0.27
WITs	6.75	0.50	16.97	0.82
WORs	0.12	0.02	0.74	0.17
WOTs	5.21	0.04	18.72	1.73

AUC = area under the curve; Ip = peak intensity; MTT = mean transit time; R^2 = the regression coefficient of the data to the model; Tp = time for peak intensity; WIR = rate of increase during wash in; WIT = wash in time; WOR = rate of decrease during wash out; WOT = wash out time.

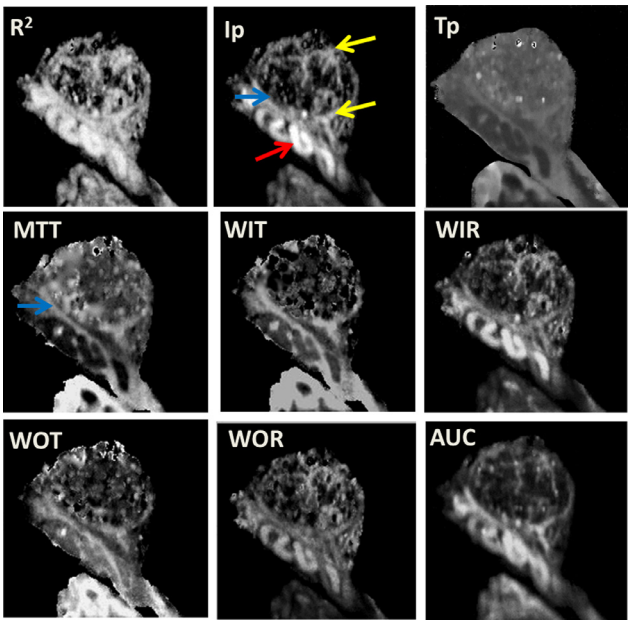

Fig. 3. Maps for each parameter calculated from TIC from 2 × 2 pixel ROIs mapping the whole image plane for CL1. The parameters that show the artery as the dominant vessel (red arrow) are the intensity-related parameters such as Ip and AUC. The time-related parameters (Tp, WIT and WOT) show the vein as the dominant vessel (blue arrow). The yellow arrows point to medium vessels. TIC = time-intensity curve; ROI = region of interest; CL = corpus luteum; Ip = peak intensity; AUC = area under the curve; Tp = time for peak intensity; WIT = wash in time; WOT = wash out time.

We have shown that large ROI analysis using CEUS is generally burdened by significant uncertainties and these should be replaced by parametric map analysis. Studies utilising TICs to assess perfusion and blood volume use large ROIs which span multiple sized vessels in an organ (Averkiou et al. 2010; Lassau et al. 2010). Given that an

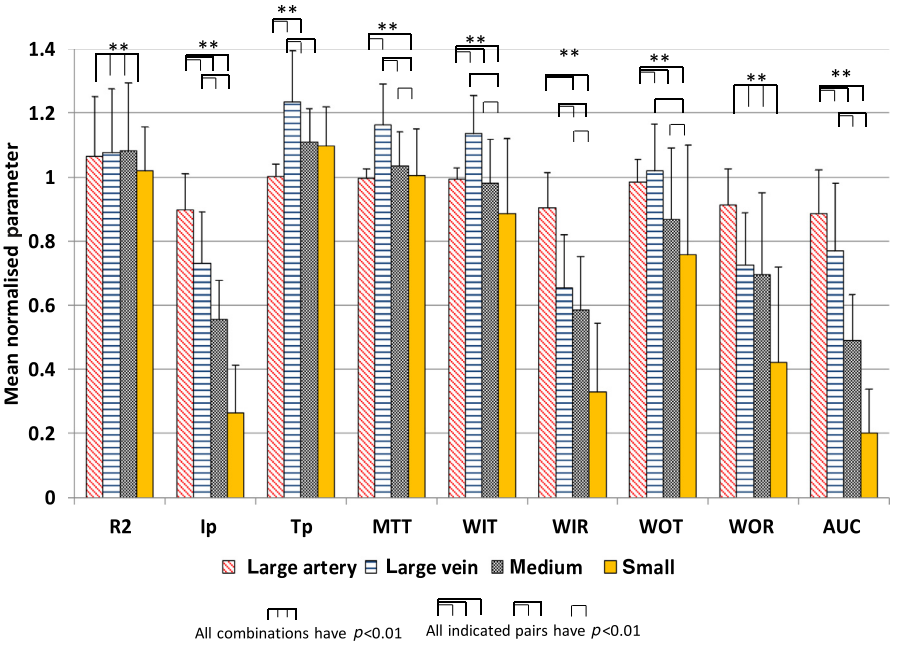

Fig. 4. Mean and standard deviation of the parameters calculated from the localised 2 × 2 pixel TIC. From ANOVA and Tukey statistical analysis, the data comparisons where significance <0.05 is indicated. As with the parameter maps in Figure 3, the intensity-related parameters were dominated by signal from arteries while time-related parameters were dominated by veins. TIC = time-intensity curve; ANOVA = analysis of variance.

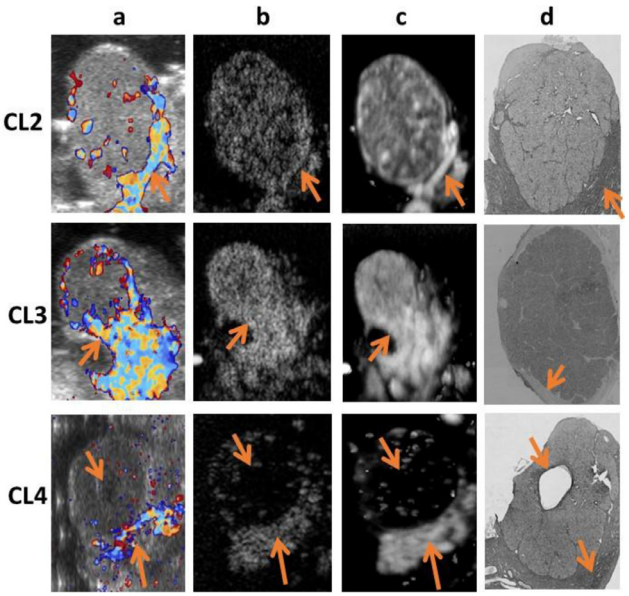

Fig. 5. Images for three different ovaries which include the colour Doppler map of the largest vessels (column a), the peak intensity frame in the contrast ultrasound scan (column b), the parametric map for peak intensity (column c) and the histology slice for the ovary (column d). The third row (CL4) shows images associated with an ovary which had been treated with prostaglandin which causes vascular regression.

ultrasound image covers large areas, including both microvasculature and larger vessels, ROI analysis, as used in Figure 1, results in erroneous estimation of most parameters compared to the values that can be found in pixel analysis. The structure of the ovine ovary enabled the deduction of vessel types in different areas of the parametric maps. The CL is a transient gland that needs to grow fast and reach maturity within 9−12 d; it has a dense central microvasculature and most importantly the larger vessels are located in the periphery of the tissue (Fig. 1b), which is clearly visible in the parametric maps. The findings here suggest that the inclusion of all vessel types in ROI analysis increases the likelihood of systematic errors, particularly for transit time−related parameters as supported by calculations of the mean difference in MTT (3.1 ± 1.8 s) and Tp (3.7 ± 1.5 s) between veins and arteries. Veins fill with contrast several seconds later, and have longer contrast transit, compared to arteries. This explains the discrepancy between ROI A and ROI B in Figure 1 and the volume-dependent calculation of transit-related parameters shown in Figure 1c. In normal tissue, millimetre-sized arteries and veins often are spatially paired, as is the case for the vessels that support the CL. Thus, the overall transit measured in a large ROI is augmented by the presence of both arterial and venous flow. The high reproducibility in WIT within the CL in repeated injections and identical scan planes was previously established to below 10% and as low as 3% (Sboros et al. 2011). The results here suggest that such low uncertainties are plausible in all tissue examinations if the kinetics of different vessels are investigated using higher resolution parametric maps.

In addition to rectifying larger vessel induced uncertainties, parametric maps could be further deployed to assess tumour perfusion kinetics. Dynamic CEUS imaging is a tool for assessing tumour perfusion (Dietrich et al. 2012). Parametric imaging has provided additional information on tumour blood volume changes, microvascular density and the assessment of vascular changes in response to treatment (Panfilova et al. 2019; Pitre-Champagnat et al. 2015; Rognin et al. 2010; Williams et al. 2011). However, to date, it has not been possible "to distinguish the different categories of vessel diameter or their maturity" (Pitre-Champagnat et al. 2015). In contrary to the CL, for most tissue types larger vessels are structurally more mixed with the microvascular bed, and it is difficult to have a clear anatomic separation between vessel types. In particular, tumours present vascular heterogeneity which makes the distinction of different vessel sizes difficult (Panfilova et al. 2019; Pitre-Champagnat et al. 2015). The work here shows that the combination of high-contrast and temporal resolution enable this delineation. By utilising all the available information from the parametric maps (Fig. 4) it is possible to effectively differentiate vessel types. The results here show that the microvascular bed has the lowest values in most calculated flow parameters apart from the MTT. Large arteries produce large values for parameters such as Ip, AUC, WIR and WOR, whereas veins dominate time-dependent parameter maps such as MTT,

WIT and WOT (Fig. 4). These are expected results. The main feeding arteries have the shortest time from injection to Ip and veins have the longest. Flow kinetics after injection produce a lower contrast agent density with time; therefore, lower echo intensities and higher transit times are found further downstream (Hudson et al. 2015). This information coupled with prior knowledge may form the basis for vessel classification in the future, even at micro-vessel level.

Vessels that are larger than the resolution limit appear to be depicted more accurately compared to colour Doppler (Fig. 5), but further work is required to establish the accuracy of sizing these vessels. The 2×2 pixel ROIs may contain more than one vessel type. Even in the case of larger, millimetre-sized, arteries and veins, it is likely that signal from other overlapping vessels is captured in the same pixels. In light of this, the hypothesis for differentiating vessel types through parametric maps refers to ROIs where the dominant signal originates from one type of vessel and likely the largest vessel in the ROI. In the example, parametric maps regions of venous flow can be differentiated from arterial flow irrespective of its direction of flow (blue and red arrows in Fig. 3).

When the size of the vessels is much smaller than the resolution of the image, their depiction will not provide an accurate measurement of their size. Each pixel is 140×140 μm (therefore the parametric map has pixel size 280×280 μm), and the ultrasound image plane has a thickness of at least 1 mm. The classification of the flow kinetics (Fig. 2) matches the broad vessel groupings in the histology, but cannot provide clarity on the sizes of the different vessel types. Figure 2c shows a strong signal and is likely to include signals from arterioles up to several tens of micrometres. Generally, micro-vessels do not provide a good fit to the lognormal model (Strouthos et al. 2010) due to their small contrast volumes that produce a noisy signal (Fig. 2c, 2d). However, the different intensity and temporal characteristics of the different vessel types should be further explored in the future to enable reproducible vessel differentiation.

The recent development of SRI (Christensen-Jeffries et al. 2015; Errico et al. 2016; O'Reilly et al. 2014; Opacic et al. 2018) may be coupled with the vessel classification proposed here. SRI promises to provide significant resolution gains in vascular mapping that may reach above 10-fold improvement (van Sloun et al. 2018). As explained in the introduction, a clinically applicable SRI method may require larger concentrations of microbubbles that ensure the image is well populated by scatter resulting in the larger vessels having very dense contrast. Therefore, hybrid methodologies may be developed that also deploy information from high-density MB distributions, such as the one presented here. Such an advance may reduce acquisition time, and thus patient examination time, by making optimal use of the available data at larger MB concentrations and the spatiotemporal information they contain. For vessels with large concentrations, a solution may be available through a largely heuristic approach proposed by Perperidis et al. by creating binary masks which highlight (as verified by associated histology slices) larger vessels (mostly around the perimetry of the CL). Yet, this approach needs to be treated with caution as it tends to overestimate the regions occupied by the medium-sized vessels.

One way to look at this is as a sparsity problem that may require a highly supervised approach. The low frame rate translates into undersampling of larger vessels with high velocities (*i.e.,* 10−15 Hz is inadequate to sample fragments of bent vessels that have blood speeds above 1 cm/s) also the microbubble transit is finite (at least 2 min). Thus, the improvement of resolution requires the deployment of prior knowledge on the vascular flow and structural properties that have to compensate the sampling problem facing SRI. Currently, the literature relies on localisation and tracking approaches with little input from prior knowledge. Deep learning has also been attempted to provide SRI and has shown promise as there was also a significant resolution gain (van Sloun et al. 2018). Knowledge on the nature of the vessels may help by providing associations between microbubble density, velocity and vessel size. In addition, traditional machine learning methodologies, adopting a classifier (such as Support Vector Machines) on a handcrafted 8-dimensional feature space (incorporating all parametric maps) (Boser et al. 1992; Pratondo et al. 2017) or custom convolutional neural networks directly on the 2-D + time data sets are anticipated to improve the classification between larger vessels and microvasculature. Binary masks and future iterations may provide hybrid methodologies that enable the identification of disease state or response to therapy, by means of automated vascular structure classification.

An important limitation in this study is the comparison with a gold standard of histology. A known consequence of tissue processing for microscopic evaluation is tissue shrinkage and shape distortion (Kerns et al. 2008). Histology evaluates slices with a thickness of a few micrometres that are physically impossible to match exactly with the ultrasound data. Ultrasound images are routinely compared with histology to evaluate prostate lesion findings. In these studies, the comparison is performed in 3-D reconstructed volumes. This process results in substantial spatial errors of a few millimetres (Wildeboer et al. 2018). Consequently, no direct quantitative comparison between the vascular structure of the CL and the ultrasound video data was performed here. Histology was used as a guide, in conjunction with well-

understood overall structure of the ovary and CL in the deduction of the vessel types.

Finally, the parameter map (CL4 Fig. 5) shows regions where vascular regression, induced by prostaglandin, has occurred. This could be used to monitor tumour regression or to locate tumour necrotic regions. The compromised vascular bed is clearly seen as a large region devoid of vascular structure. Specifically, and as noted in the results section, it is the lack of medium vessels in the central region which indicates the absence of vascular structure. It is known that better knowledge of the flow characteristics of ultrasound contrast agent through a vascular network can aid in diagnosis (Eisenbrey et al. 2013). TIC analysis has been previously shown to be a good method by which to assess vascular regression of tumours in a range of solid tumour types (Lassau et al. 2014; Lassau et al. 2012). AUC has been shown to be the most significant parameter for indication of tumour stability when the whole tumour was selected as the ROI (Lassau et al. 2014). The use of all available pixel kinetics information may lead to improved characterisation of therapeutic vascular regression.

CONCLUSIONS

This study demonstrates the ability of parametric maps, across a regular grid of TICs, derived from CEUS frame sequences, to assist in the visual differentiation of different vessel types, including arteries, veins and capillaries. Parameters associated with the differentiation of specific structures have been identified. Furthermore, parametric mapping has demonstrated the potential to indicate regions where vascular regression has occurred and can potentially be used to monitor tumour regression. Classification algorithms can potentially use this information to generate binary masks differentiating microvasculature from larger vessels, thus potentially enriching current super-resolution methodologies with much needed prior knowledge.

Acknowledgments—The authors wish to acknowledge funding from the Medical Research Council (UK) (G0800896), the Science and Technology Facilities Council (UK) (ST/M007804/1) and the British Heart Foundation (PG/10/021/28254) that made this work possible. M.A. would like to Life Sciences Discovery Fund 3292512 and the Department of Defense DOD-CDMRP CA160415/PRCRP.

REFERENCES

Averkiou M, Lampaskis M, Kyriakopoulou K, Skarlos D, Klouvas G, Strouthos C, Leen E. Quantification of tumor microvascularity with respiratory gated contrast enhanced ultrasound for monitoring therapy. Ultrasound Med Biol 2010;36:68–77.

Baird DT, McNeilly AS. Gonadotrophic control of follicular development and function during the oestrous cycle of the ewe. J Reprod Fertil Suppl 1981;30:119–133.

Boser BE, Guyon IM, Vapnik VN. A training algorithm for optimal margin classifiers. In: Proceedings of the Fifth Annual Workshop on Computational Learning Theory. Pittsburgh, Pennsylvania, USA. ACM press; 1992. p. 144–151.

Christensen-Jeffries K, Browning RJ, Tang MX, Dunsby C, Eckersley RJ. *In vivo* acoustic super-resolution and super-resolved velocity mapping using microbubbles. IEEE Trans Med Imaging 2015;34:433–440.

Dietrich CF, Averkiou MA, Correas JM, Lassau N, Leen E, Piscaglia F. An EFSUMB introduction into dynamic contrast-enhanced ultrasound (DCE-US) for quantification of tumour perfusion. Ultraschall Med 2012;33:344–351.

Dijkmans PA, Knaapen P, Sieswerda GT, Aiazian E, Visser CA, Lammertsma AA, Visser FC, Kamp O. Quantification of myocardial perfusion using intravenous myocardial contrast echocardiography in healthy volunteers: Comparison with positron emission tomography. J Am Soc Echocardiogr 2006;19:285–293.

Dizeux A, Payen T, Le Guillou-Buffello D, Comperat E, Gennisson JL, Tanter M, Oelze M, Bridal SL. *In Vivo* multiparametric ultrasound imaging of structural and functional tumor modifications during therapy. Ultrasound Med Biol 2017;43:2000–2012.

Eisenbrey JR, Wilson CC, Ro RJ, Fox TB, Liu JB, Chiou SY, Forsberg F. Correlation of ultrasound contrast agent derived blood flow parameters with immunohistochemical angiogenesis markers in murine xenograft tumor models. Ultrasonics 2013;53:1384–1391.

El-Galaly TC, Gormsen LC, Hutchings M. PET/CT for staging: Past, present, and future. Semin Nucl Med 2018;48:4–16.

Errico C, Osmanski BF, Pezet S, Couture O, Lenkei Z, Tanter M. Transcranial functional ultrasound imaging of the brain using microbubble-enhanced ultrasensitive Doppler. Neuroimage 2016;124:752–761.

Errico C, Pierre J, Pezet S, Desailly Y, Lenkei Z, Couture O, Tanter M. Ultrafast ultrasound localization microscopy for deep super-resolution vascular imaging. Nature 2015;527:499–502.

Folkman J. Angiogenesis and apoptosis. Semin Cancer Biol 2003;13:159–167.

Forsberg F, Ro RJ, Fox TB, Liu JB, Chiou SY, Potoczek M, Goldberg BB. Contrast enhanced maximum intensity projection ultrasound imaging for assessing angiogenesis in murine glioma and breast tumor models: A comparative study. Ultrasonics 2011;51:382–389.

Fraser HM, Duncan WC. SRB Reproduction, Fertility and Development Award Lecture 2008. Regulation and manipulation of angiogenesis in the ovary and endometrium. Reprod Fertil Dev 2009;21:16.

Greis C. Quantitative evaluation of microvascular blood flow by contrast-enhanced ultrasound (CEUS). Clin Hemorheol Microcirc 2011;49:137–149.

Hudson JM, Williams R, Tremblay-Darveau C, Sheeran PS, Milot L, Bjarnason GA, Burns PN. Dynamic contrast enhanced ultrasound for therapy monitoring. Eur J Radiol 2015;84:1650–1657.

Kerns MJ, Darst MA, Olsen TG, Fenster M, Hall P, Grevey S. Shrinkage of cutaneous specimens: Formalin or other factors involved?. J Cutan Pathol 2008;35:1093–1096.

Kuenen MPJ, Mischi M, Wijkstra H. Contrast-ultrasound diffusion imaging for localization of prostate cancer. IEEE Trans Med Imaging 2011;30:1493–1502.

Kuenen MPJ, Saidov TA, Wijkstra H, Mischi M. Contrast-ultrasound dispersion imaging for prostate cancer localization by improved spatiotemporal similarity analysis. Ultrasound in Med Biol 2013;39:1631–1641.

Lagaru A, Gambhir SS. Imaging tumor angiogenesis: The road to clinical utility. AJR Am J Roentgenol 2013;201:W183–W191.

Lassau N, Bonastre J, Kind M, Vilgrain V, Lacroix J, Cuinet M, Taieb S, Aziza R, Sarran A, Labbe-Devilliers C, Gallix B, Lucidarme O, Ptak Y, Rocher L, Caquot LM, Chagnon S, Marion D, Luciani A, Feutray S, Uzan-Augui J, Coiffier B, Benastou B, Koscielny S. Validation of dynamic contrast-enhanced ultrasound in predicting outcomes of antiangiogenic therapy for solid tumors: The French multicenter support for innovative and expensive techniques study. Invest Radiol 2014;49:794–800.

Lassau N, Chapotot L, Benatsou B, Vilgrain V, Kind M, Lacroix J, Cuinet M, Taieb S, Aziza R, Sarran A, Labbe C, Gallix B, Lucidarme O, Ptak Y, Rocher L, Caquot LM, Chagnon S, Marion D, Luciani A, Uzan-Augui J, Koscielny S. Standardization of dynamic

contrast-enhanced ultrasound for the evaluation of antiangiogenic therapies: The French multicenter Support for Innovative and Expensive Techniques Study. Invest Radiol 2012;47:711–716.
Lassau N, Koscielny S, Albiges L, Chami L, Benatsou B, Chebil M, Roche A, Escudier BJ. Metastatic renal cell carcinoma treated with sunitinib: Early evaluation of treatment response using dynamic contrast-enhanced ultrasonography. Clin Cancer Res 2010;16:1216–1225.
Lewis JP. Fast template matching. Vision Interface 1995;95:15–19.
Moreno PR, Purushothaman KR, Sirol M, Levy AP, Fuster V. Neovascularization in human atherosclerosis. Circulation 2006;113:2245–2252.
Mori N, Mugikura S, Takahashi S, Ito K, Takasawa C, Li L, Miyashita M, Kasajima A, Mori Y, Ishida T, Kodama T, Takase K. Quantitative analysis of contrast-enhanced ultrasound imaging in invasive breast cancer: A novel technique to obtain histopathologic information of microvessel density. Ultrasound Med Biol 2017;43:607–614.
Nelder JA, Mead R. A simplex method for function minimization. Comput J 1965;7:308–313.
O'Reilly MA, Jones RM, Hynynen K. Three-dimensional transcranial ultrasound imaging of microbubble clouds using a sparse hemispherical array. IEEE Trans Biomed Eng 2014;61:1285–1294.
Opacic T, Dencks S, Theek B, Piepenbrock M, Ackermann D, Rix A, Lammers T, Stickeler E, Delorme S, Schmitz G, Kiessling F. Motion model ultrasound localization microscopy for preclinical and clinical multiparametric tumor characterization. Nat Commun 2018;9:1527.
Panfilova A, Shelton SE, Caresio C, van Sloun RJG, Molinari F, Wijkstra H, Dayton PA, Mischi M. On the relationship between dynamic contrast-enhanced ultrasound parameters and the underlying vascular architecture extracted from acoustic angiography. Ultrasound Med Biol 2019;45:539–548.
Perperidis A, Thomas D, Averkiou M, Duncan C, McNeilly A, Butler M, Sboros V. 2014 Automatic dissociation between microvasculature and larger vessels for ultrasound contrast imaging. 36th Annual International Conference of the IEEE Engineering in Medicine and Biology Society. New York: IEEE; 2014. p. 5076–5079.
Pitre-Champagnat S, Leguerney I, Bosq J, Peronneau P, Kiessling F, Calmels L, Coulot J, Lassau N. Dynamic contrast-enhanced ultrasound parametric maps to evaluate intratumoral vascularization. Invest Radiol 2015;50:212–217.
Pratondo A, Chui C, Ong S. Integrating machine learning with region-based active contour models in medical image segmentation. J Vis Commun Image Represent 2017;43:1–9.
Rognin NG, Arditi M, Mercier L, Frinking PJ, Schneider M, Perrenoud G, Anaye A, Meuwly JY, Tranquart F. Parametric imaging for characterizing focal liver lesions in contrast-enhanced ultrasound. IEEE Trans Ultrason Ferroelectr Freq Control 2010;57:2503–2511.
Saidov T, Heneweer C, Kuenen M, von Broich-Oppert J, Wijkstra H, Rosette JDL, Mischi M. Fractal dimension of tumor microvasculature by DCE-US: Preliminary study in mice. Ultrasound Med Biol 2016;42:2852–2863.
Sboros V. 2014 The ovine corpus luteum angiogenesis model: A tool for developing imaging technology. 36th Annual International Conference of the IEEE Engineering in Medicine and Biology Society. New York: IEEE; 2014. p. 4280–4282.
Sboros V, Averkiou M, Lampaskis M, Thomas DH, Silva N, Strouthos C, Docherty J, McNeilly AS. Imaging of the ovine corpus luteum microcirculation with contrast ultrasound. Ultrasound Med Biol 2011;37:59–68.
Sboros V, Moran CM, Pye SD, McDicken WN. The behaviour of individual contrast agent microbubbles. Ultrasound Med Biol 2003;29:687–694.
Simoncic U, Leibfarth S, Welz S, Schwenzer N, Schmidt H, Reischl G, Pfannenberg C, Fougère C, Nikolaou K, Zips D, Thorwarth D. Comparison of DCE−MRI kinetic parameters and FMISO−PET uptake parameters in head and neck cancer patients. Med Phys 2017;44:2358–2368.
Strouthos C, Lampaskis M, Sboros V, Mcneilly A, Averkiou M. Indicator dilution models for the quantification of microvascular blood flow with bolus administration of ultrasound contrast agents. IEEE Trans Ultrason Ferroelectr Freq Control 2010;57:1296–1310.
van Sloun RJG, Demi L, Schalk SG, Caresio C, Mannaerts C, Postema AW, Molinari F, van der Linden HC, Huang P, Wijkstra H, Mischi M. Contrast-enhanced ultrasound tractography for 3 D vascular imaging of the prostate. Sci Rep 2018;8:14640.
van Sloun RJG, Solomon O, Bruce M, Khaing ZZ, Eldar YC, Mischi M. Deep Learning for Super-resolution Vascular Ultrasound Imaging. IEEE International Conference on Acoustics, Speech and Signal Processing (ICASSP). New York: IEEE; 2019. p. 1055–1059.
Vonnahme KA, Redmer DA, Borowczyk E, Bilski JJ, Luther JS, Johnson ML, Reynolds LP, Grazul-Bilska AT. Vascular composition, apoptosis, and expression of angiogenic factors in the corpus luteum during prostaglandin F2 alpha-induced regression in sheep. Reproduction 2006;131:1115–1126.
Wildeboer RR, van Sloun RJG, Postema AW, Mannaerts CK, Gayet M, Beerlage HP, Wijkstra H, Mischi M. Accurate validation of ultrasound imaging of prostate cancer: A review of challenges in registration of imaging and histopathology. J Ultrasound 2018;21:197–207.
Williams R, Hudson JM, Lloyd BA, Sureshkumar AR, Lueck G, Milot L, Atri M, Bjarnason GA, Burns PN. Dynamic microbubble contrast-enhanced US to measure tumor response to targeted therapy: A proposed clinical protocol with results from renal cell carcinoma patients receiving antiangiogenic therapy. Radiology 2011;260:581–590.